Scripta Materialia 163 (2019) 62–65

Contents lists available at ScienceDirect

Scripta Materialia

journal homepage: www.elsevier.com/locate/scriptamat

Examination of B in the Mo solid solution (Mo_{ss}) in $Mo_{ss} + Mo_5SiB_2 + Mo_2B$ alloys

Longfei Liu [a], Congli Sun [a], Chenyu Zhang [a], Paul M. Voyles [a], John Fournelle [b], Anette Handt [c], John H. Perepezko [a,*]

[a] Department of Materials Science and Engineering, University of Wisconsin-Madison, 1509 University Ave., Madison, WI 53706, USA
[b] Department of Geoscience, University of Wisconsin-Madison, 1215 West Dayton Street, Madison, WI 53706, USA
[c] Department of Earth Sciences, University of Minnesota, 116 Church St. SE, Minneapolis, MN 55455, USA

ARTICLE INFO

Article history:
Received 20 November 2018
Received in revised form 31 December 2018
Accepted 1 January 2019
Available online xxxx

Keywords:
Refractory metals
Scanning/transmission electron microscopy (STEM)
Solid solubility
Interstitials

ABSTRACT

During an examination of the Mo_{ss} (Mo solid solution) + Mo_5SiB_2 + Mo_2B three phase alloys a lattice constant expansion was observed for the Mo_{ss}. To identify the origin of the expansion, high precision analysis of scanning transmission electron microscopy images was carried out to determine the solid solution type of B atoms. A quantitative analysis of the non-rigid registration image demonstrates that the B is located at the octahedral sites of the Mo lattice. This conclusion is consistent with the expansion of lattice constant and the small solid solubility limit of B in Mo_{ss}.

Recently, considerable effort has been devoted to the development of ultra-high temperature structural materials as alternatives to Ni-based superalloys in order to improve the energy efficiency of gas turbine systems [1–3]. Among the several potential candidates, Mo-Si-B alloys have drawn much attention due to their high melting point and high temperature strength [4–6].

In the Mo-Si-B system, nearly all the research has focused on the Mo-rich corner, especially the $Mo_{ss} + Mo_5SiB_2$ (T_2) + Mo_3Si three phase region [7–20]. Based upon thermodynamic calculations the Mo_{ss} in this three phase region has a Si solubility of about 2.1 at.% Si (1600 °C) and 2.6 at.% Si (1800 °C) [26]. Silicon is a known potent solid solution hardener in Mo [4,6]. It is believed that due to Si in the α-Mo phase, the Mo-Si-B system suffers from extensive work hardening and loss of ductility at room temperature [22–25]. Thus, strategies to lower the Si content in the Mo_{ss} phase can be a key to improve the ductility and toughness of Mo-Si-B alloys [22–25]. One approach to reduce the Si solubility is to examine the $Mo_{ss} + T_2 + Mo_2B$ three phase region. In this three phase region, the Si solid solubility limit in Mo is calculated as about 1.38 at.% (1600 °C) and 1.75 at.% Si (1800 °C) [26] which is lower than the values in the $Mo_{ss} + T_2 + Mo_3Si$ three phase region. Calculated phase diagram sections based upon the Pandat database [26] shown in Fig. 1a highlight the difference of Si content in the Mo_{ss} between $Mo_{ss} + T_2 + Mo_3Si$ three phase region and $Mo_{ss} + T_2 + Mo_2B$ three phase region. As in the $Mo_{ss} + T_2 + Mo_3Si$ three phase alloys, where the T_2 phase provides the oxidation resistance, it is expected that the T_2 phase can act similarly in the $Mo_{ss} + T_2 + Mo_2B$ three phase region. However, the solid solution type and effect of B atoms in the Mo_{ss}, are unknown, but are fundamental in determining the Mo_{ss} properties [27].

The boron solubility in the Mo_{ss} in the Mo-B binary system has been reported to have values between 0.2 at.% B and 1.75 at.% B at the eutectic temperature [28–31]. All of these reported values are based upon a test method involving metallographic analysis on annealed Mo samples with a specific B content to determine whether there is the presence of a secondary phase. This method is limited in capability to determine a low B content which is below 0.1 at.% [28] (Supplementary Material.1).

In this study, in order to elucidate the solid solution behavior X-ray diffraction (XRD), Scanning Electron Microscopy (SEM), Electron Probe Microanalysis (EPMA) and Scanning transmission electron microscopy (STEM) were used to examine Mo_{ss} + T2 + Mo_2B three phase alloys with compositions bordering the $Mo_{ss} + T_2$ two phase field.

Six alloy ingots were prepared by repetitive arc-melting of pure Mo (99.95 wt%), Si (99.99 wt%) and B (99.95 wt%) in a water-cooled Cu mold under a Ti gettered Ar atmosphere. The ingots were re-melted 5 times to achieve a homogeneous element distribution. For these six alloys, four of them are ternary alloys along the red line in Fig. 1b, the other two are binary alloys. The nominal compositions of the ternary samples are Mo-xSi-(2.2x − 2.8)B (x = 3, 5, 7, 9) which are shown in

* Corresponding author.
E-mail address: perepezk@engr.wisc.edu (J.H. Perepezko).

https://doi.org/10.1016/j.scriptamat.2019.01.003
1359-6462/

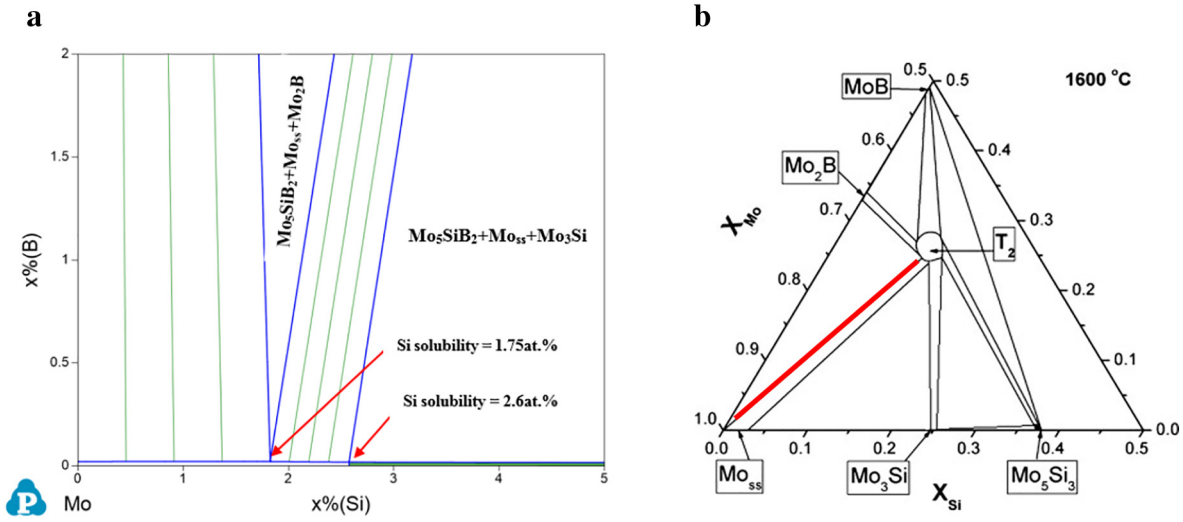

Fig. 1. Mo-Si-B isothermal phase diagrams. a) Calculated Mo-rich corner at 1800 °C, b) Mo-rich corner at 1600 °C.

the partial Mo-Si-B ternary phase diagram in Fig. 1b, and the binary samples are Mo-2B and Mo-1.75Si.

All heat treatments were carried out at 1800 °C for 50 h in an Ar atmosphere.

The crystalline phases of all samples were identified by X-ray diffractometry (Bruker D8 Advance). The chemical compositions of constituent phases in the studied alloys were measured using CAMECA SX51 and SXFiveFE electron microprobes operated at an accelerating voltages of 6 or 7 kV and a current density of between 6 and 20 × 10^{-9} A [32]. Calibration standards consisted of 99.99% pure Mo, Si and B. Samples and standards were mounted in a conductive media and not coated. The probe sizes ranging from the finest available (<1 μm) up to 10–20 μm were used to measure the compositions of constituent phases and solidified zones (with a fine-scale solidification microstructure), respectively. The accuracy of the experimental compositions was evaluated using the "analytical total" reliability test, before any normalized atomic values were accepted. Only the EPMA compositions, where the non-normalized weight percent totals were in the range from 98.5 to 101 wt%, were accepted. The minimum detection limit for B is 0.011 wt% which is equivalent to 0.098 at.% B. The full details of the EPMA measurements and analysis are covered in the supplementary materials.

The annealed samples were examined by electron backscatter diffraction (EBSD, EDAX Hikari EBSD Camera) to determine grain orientations. For the BCC crystal, the tetrahedral sites and octahedral sites are not overlapped by vertical viewing through the (111) plane, which is the ideal surface for STEM examination. The finely polished sample surface was examined by EBSD to find the working ($1\bar{1}0$) plane which is vertical to the desired (111) plane. Atomic-resolution scanning transmission electron microscopy (STEM) imaging was performed on a FEI Titan microscope equipped with CEOS probe aberration corrector operated at 200 kV. Annular bright field (ABF) images were collected with a 24.5-mrad probe semi-angle, 20 pA probe current, STEM resolution of ~0.9 Å and detector range of 5.7–22.8 mrad. An image series with 150 frames was acquired with 1 s/frame frequency and post-processed with non-rigid registration to compensate for drift between frames. During registration, all frames were referenced to the first frame and this process was iterated several times to reach a final registration. To avoid being trapped by local minimum in the nearly periodic STEM images, a coarse-to-fine multilevel approach was used to first register image at coarse level [33]. At each level, the minimization problem was solved by using a regularized gradient descent method. The registered image series was averaged to get a single image with high signal-to-noise ratio. The image was then cropped to use a subset that contains information from all 150 frames.

The microstructure of the annealed Mo-5Si-8.2B sample is shown in Fig. 2, where the lighter color phase is Mo_{ss}, the darker color phase is T_2 and the minor Mo_2B phase is revealed in the insert. EPMA measurements of each phases indicated that the Mo_{ss} has 1.75 ± 0.08 at.% Si but B is below the detection limit of 0.1 at.%. The T_2 phase has 26.10 ± 0.80 at.% B, 11.12 ± 0.43 at.% Si and 62.77 ± 0.69 at.% Mo. The XRD results for all samples are shown in Fig. S1 along with the enlarged spectra between 38° and 43°. Since the composition of all samples is far away from the Mo_2B corner, the phase fraction of Mo_2B in all samples is negligible, so that there is no obvious peak for the Mo_2B phase in the XRD results. The lattice parameters of Mo_{ss} are calculated based on XRD results and are shown in Table 1.

The lattice constant of pure Mo was measured as 3.14701 ± 3 × 10^{-5} Å, and agrees with the value in the ICDD (International Center for Diffraction Data) database. The lattice constants for the binary alloys in Table 1 represent saturation values. The results in Table 1 show that the average of the Moss lattice constants in all ternary alloys is larger than that for pure Mo which means that the net result of the addition

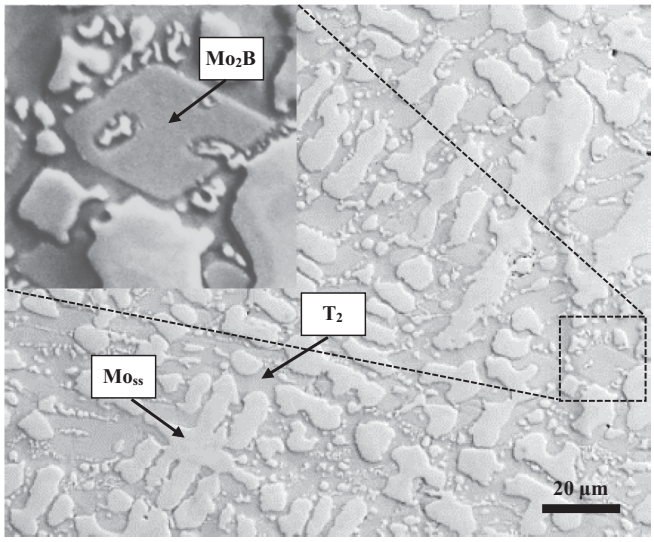

Fig. 2. Microstructure of Mo-5Si-8.2B alloy after 50 h 1800 °C annealing.

Table 1
Calculated lattice parameters of Mo_{ss} for all samples based on XRD results. Compositions are in atomic percent.

Sample	Solute in Mo_{ss} (at.%)	Lattice parameter (Å)
Mo-xSi-(2.2x − 2.8)B (x = 3–9)	1.75Si + 0.1B	$3.14987 \pm 2 \times 10^{-5}$
Mo-1.75Si	1.75Si	$3.14648 \pm 5 \times 10^{-5}$
Mo-2B	0.1B	$3.15323 \pm 2 \times 10^{-5}$

of B and Si is to expand the Mo lattice. Many previous results showed that the addition of Si in Mo_{ss} will reduce the lattice constant, so that the Si atoms are substitutional in Mo_{ss} [21]. Since both the Si and B are saturated in the Mo_{ss} the lattice parameter reduction due to Si is more than compensated by the lattice parameter increase due to B. The mean lattice parameter of Mo_{ss} in all Mo-Si-B samples is $3.14987 \pm 2 \times 10^{-5}$ Å, the lattice parameter of Mo-1.75Si is $3.14648 \pm 5 \times 10^{-5}$ Å and the lattice parameter of Mo-2B is $3.15323 \pm 2 \times 10^{-5}$ Å. These values can be used to calculate the combined effect of both Si and B to the lattice parameter of Mo-Si-B alloy, by Eq. (1)

$$a_{Mo_{ss}} = a_{Mo} + X_B \frac{da}{dX_B} + X_{Si} \frac{da}{dX_{Si}} + a_{Si+B\ interaction} \quad (1)$$

a_i is the lattice parameter of i, X_j is the solubility of j in Mo_{ss}. The left side of Eq. (1) is the lattice parameter of the Mo solid solution, and the four terms of the right side of Eq. (1) are the lattice parameter of pure Mo, the effect of B, the effect of Si and Si and B interaction effect, respectively. The data listed in Table 1 are used for the calculation as 3.14701 Å for a_{Mo}, 0.1 at.% for X_B from the EPMA result, 6.234×10^{-2} Å/at.% for $\frac{da}{dX_B}$, 1.75 at.% for X_{Si} [26], 2.972×10^{-4} Å/at.% for $\frac{da}{dX_{Si}}$, respectively. Based on the data above, the calculated $a_{Mo_{ss}}$ is 3.14985 Å+$a_{Si+B\ interaction}$, and the mean lattice parameter of all Mo-Si-B samples is 3.14987 Å, so that the $a_{Si+B\ interaction}$ is nearly zero. The result means that the Si and B act independently in changing the Mo_{ss} lattice parameter.

The above results and previous publications [28] suggest that B atoms could occupy interstitial sites in Mo_{ss} and have a larger effect on the lattice constant change than Si. Since the B solid solubility limit in Mo_{ss} at 1800 °C is about 0.1 at.% [28], all ternary samples have more B content than the solubility limit and will form saturated solid solutions (same lattice constant) at equilibrium. The expansion of the lattice constant and small solid solubility limit are two reasons that B may reside in interstitial sites in Mo_{ss}.

The experimental procedure for the STEM examination is shown in Fig. 3. First, the Mo-3Si-3.8B ingot was annealed at 1800 °C for 50 h to form sub-millimeter grains, then the finely polished sample surface was examined by EBSD to find the working $(1\bar{1}0)$ plane (dark blue area) which is vertical to the desired (111) plane. Vertical cutting can deliver the best quality STEM sample and finally a 5 nm thin layer, which was prepared by focused ion beam (FIB), was examined by STEM.

Fig. 4 shows the STEM result of Mo-3Si-3.8B sample. Fig. 4a is the averaged image of 150 frames after fitting. The analysis method was developed by Yankovich et al. [33] and the result can be used for quantitative measurement of atom locations in crystals. On the ABF-STEM image (Fig. 4a), atom sites appear as dark spots on a bright background, and the repeating hexagonal structure is the Mo lattice. The line scan of the non-rigid registration ABF- STEM image in Fig. 4a is given in Fig. 4b and there are two obvious minima (minimum 1 and minimum 2) which indicate there are atoms in those positions in the Mo BCC structure. The line scan in Fig. 4b shows the intensity trend of the white line in Fig. 4a from bottom to top, the x axis is the pixel number and the y axis is the intensity. With the pixel number of minima 1 and minima 2, the relative positions of those two points can be marked in the enlarged image (Fig. 4c). Fig. 4d shows the tetrahedral and octahedral sites in the BCC crystal on the (111) surface. The white circle is the Mo atom, the green dot O is the octahedral site in the Mo BCC crystal and the green dot T is the tetrahedral site in the Mo BCC crystal. The midpoint of 2 Mo atoms is the octahedral site and near the center of the triangle is the tetrahedral site. From Fig. 4b and c, the B atoms can be determined to reside on the octahedral sites (point 1 and point 2 in Fig. 4c). The ABF-STEM intensity on the tetrahedral sites (center of Mo atoms triangles) ranges between 4.98×10^4 and 5.06×10^4 which is higher than the possible site of B (middle of two Mo atoms), as B will decrease intensity to around 4.6×10^4 (see Fig. 4b).

In the BCC Mo crystal, the tetrahedral site radius is 42.20 pm and the octahedral site radius is 22.33 pm. The tetrahedral site is bigger than the octahedral site, but both of these sites are not big enough for a boron atom (85 pm). Due to the site size difference, a boron atom would be expected to prefer to occupy the tetrahedral site in the Mo crystal. The

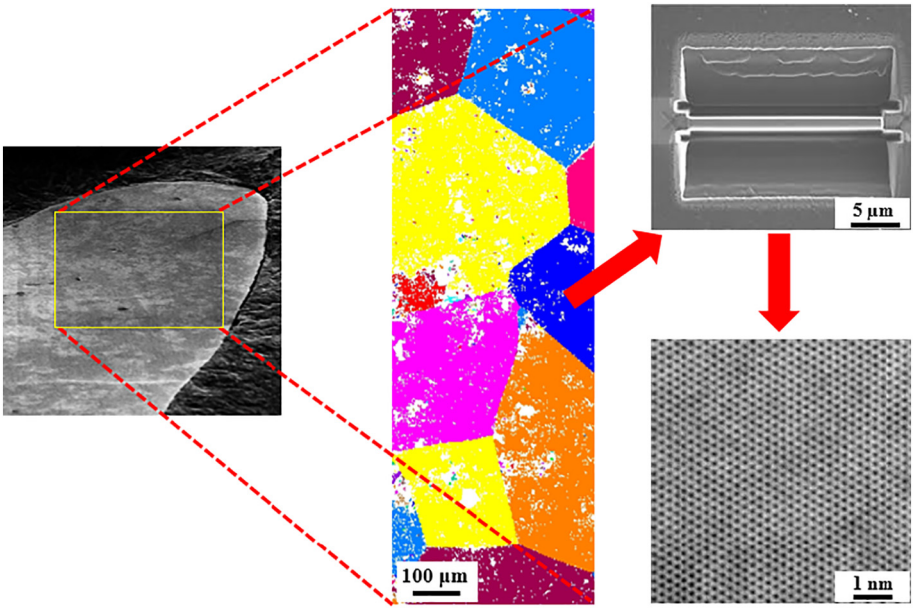

Fig. 3. Procedure of STEM test for Mo-3Si-3.8B: a) the Mo-3Si-3.8B ingot was annealed at 1800 °C for 50 h to form sub-millimeter grains, b) the finely polished sample surface was examined by EBSD to find the $(1\bar{1}0)$ plane (dark blue area), c) a 5 nm thin layer which was prepared by focused ion beam (FIB), d) sample was examined by STEM. (For interpretation of the references to color in this figure legend, the reader is referred to the web version of this article.)

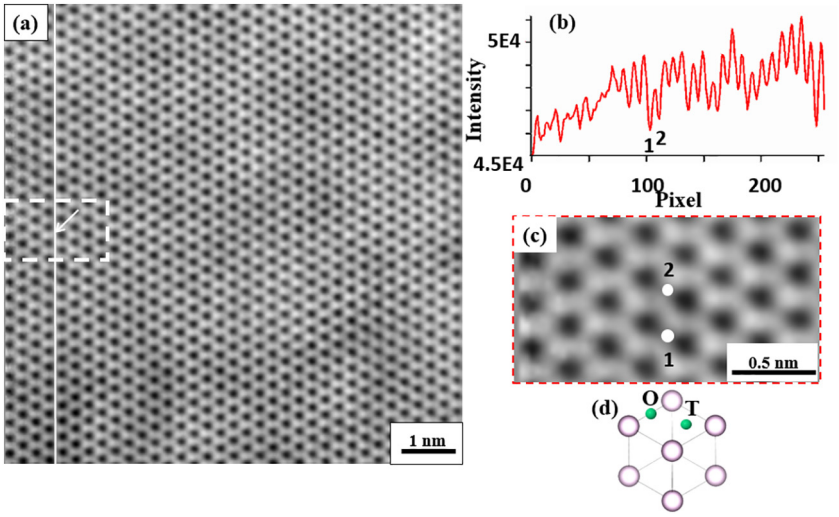

Fig. 4. STEM image of Mo-3Si-3.8B. a) averaged image of 150 frames after non-rigid registration, b) line scan of the possible interstitial solute locations, c) enlarged image of selected area, d) tetrahedral (T) and octahedral (O) sites in the BCC crystal on the (111) surface.

inconsistency of experimental result and site size calculation may be explained due to the fact that the octahedral site has six neighboring atoms compared to the tetrahedral site with only four neighbor atoms. The greater number of neighbor atoms for the octahedral site can facilitate stress relaxation and may reduce the global energy of the whole system (supplementary materials) [34].

Moreover, the Hägg rule can be used to predict whether there can be an interstitial solid solution [35]. The Hägg rule states that if the ratio (R) of the metalloid atom radius to the metal atom radius satisfies $R < 0.59$, a solid solution will form in which the metalloid occupies interstitial sites in a metal lattice. The atom radius of Mo is 145 pm and the atom radius of B is 85 pm, due to this the ratio (R) is 0.586 which is close to the Hägg limit. Accordingly, B can occupy the interstitial site in Mo ($R < 0.59$) but with a small solubility.

In summary, from an examination of a series of alloys in the $Mo_{ss} + T_2 + Mo_2B$ three phase region, the Mo_{ss} in this three phase region has a lower Si solid solubility limit than in the $Mo_{ss} + T_2 + Mo_3Si$ phase region. The XRD results show a lattice constant expansion for Mo_{ss}. Analysis of STEM images with pm-precision was carried out to determine the solid solution type of B atom in Mo_{ss} and quantitative analysis of non-rigid registration image shows that the B atoms occupy the octahedral interstitial sites. This conclusion is consistent with the expansion of the lattice constant and the low solid solubility limit of B in Mo_{ss}.

Acknowledgement

The support from the Air Force Office of Scientific Research (FA9550-17-1-0057) is gratefully acknowledged.

Appendix A. Supplementary data

Supplementary data to this article can be found online at https://doi.org/10.1016/j.scriptamat.2019.01.003.

References

[1] D.M. Dimiduk, J.H. Perepezko, MRS Bull. 28 (2003) 639–645.
[2] J.H. Perepezko, Science 326 (2009) 1068–1069.
[3] W.O. Soboyejo, T.S. Srivatsan (Eds.), Advanced Structural Materials: Properties, Design Optimization, and Applications, CRC press, Boca Raton, 2006.
[4] P. Jain, K.S. Kumar, Acta Mater. 58 (2010) 2124–2142.
[5] S. Burk, G. Bronislava, C. Hans-Jürgen, Acta Mater. 58 (2010) 6154–6165.
[6] P. Jain, K.S. Kumar, Scr. Mater. 62 (2010) 1–4.
[7] H. Nowotny, R. Kieffer, F. Benesovsky, Planseeber Pulvermet. 5 (1957) 86–93.
[8] H. Nowotny, E. Dimakopoulou, H. Kudielka, Monatsh. Chem. 88 (2) (1957) 180–192.
[9] R. Sakidja, J.H. Perepezko, S. Kim, N. Sekido, Acta Mater. 56 (2008) 5223–5244.
[10] R. Sakidja, J.H. Perepezko, Metall. Mater. Trans. A 36 (2005) 507–514.
[11] S. Kim, J.H. Perepezko, J. Phase Equilib. Diffus. 27 (2006) 605–613.
[12] R. Sakidja, J.H. Perepezko, J. Nucl. Mater. 366 (2007) 407–416 (2).
[13] N. Sekido, R. Sakidja, J.H. Perepezko, Intermetallics 15 (2007) 1268–1276.
[14] F.A. Rioult, S.D. Imhoff, R. Sakidja, J.H. Perepezko, Acta Mater. 57 (2009) 4600–4613.
[15] J. Schmelzer, S.K. Rittinghaus, A. Weisheit, M. Stobik, J. Paulus, K. Gruber, E. Wessel, C. Heinze, M. Krüger, Int. J. Refract. Met. Hard Mater. 78 (2019) 123–126.
[16] S.K. Makineni, A.R. Kini, E.A. Jägle, H. Springer, D. Raabe, B. Gault, Acta Mater. 151 (2018) 31–40.
[17] J. Wang, B. Li, R. Li, T. Wang, X. Chen, G. Zhang, Ceram. Int. 45 (2019) 3111–3117.
[18] Y. Yang, Y.A. Chang, L. Tan, W. Cao, Acta Mater. 53 (2005) 1711–1720.
[19] G. Hasemann, D. Kaplunenko, I. Bogomol, M. Krüger, JOM-US 68 (2016) 2847–2853.
[20] M. Heilmaier, M. Krüger, H. Saage, J. Rösler, D. Mukherji, U. Glatzel, R. Völkl, JOM-US 61 (2009) 61–67.
[21] J.A. Lemberg, R.O. Ritchie, Adv. Mater. 24 (2012) 3445–3480.
[22] D. Sturm, M. Heilmaier, Joachim H. Schneibel, P. Jéhanno, Birgit Skrotzki, H. Saage, Mater. Sci. Eng. A 463 (2007) 107–114.
[23] M.K. Miller, E.A. Kenik, M.S. Mousa, K.F. Russell, A.J. Bryhan, Scr. Mater. 46 (2002) 299–303.
[24] M.K. Miller, A.J. Bryhan, Mater. Sci. Eng. A 327 (2002) 80–83.
[25] H. Saage, M. Krüger, D. Sturm, M. Heilmaier, J.H. Schneibel, E. George, L. Heatherly, Ch. Somsen, G. Eggeler, Y. Yang, Acta Mater. 57 (2009) 3895–3901.
[26] Pandat, Software Package for Multi-component Phase Diagram Calculation, Developed by CompuTherm LLC, 437 S. Yellowstone Dr., Madison, WI 53719, USA, 1999.
[27] E.N. Ageeva, M.M. Kantor, S.B. Maslenkov, I.V. Korkin, Met. Sci. Heat Treat. 30 (1988) 225–229.
[28] V.I. Kharitonov, M.S. Makunin, F.I. Shamray, Russ. Metall. 3 (1971) 113–116.
[29] Y.C. Chuang, T.L. Chuang, C.H. Wu, Sci. Sinica 13 (1964) 1851.
[30] K.I. Portnoi, Y.V. Levinskii, V.M. Romashov, O.A. Morovin, M.K. Levinskaya, Izv. Akad. Nauk SSSR, Met. 4 (1967) 171.
[31] V.I. Kharitonov, M.S. Makunin, F.I. Shamarai, Tsvetn. Metall. 41 (1968) 84.
[32] J.H. Fournelle, S. Kim, J.H. Perepezko, Surf. Interface Anal. 37 (2005) 1012–1016.
[33] A.B. Yankovich, B. Berkels, W. Dahmen, P. Binev, S.I. Sanchez, S.A. Bradley, A. Li, I. Szlufarska, P.M. Voyles, Nat. Commun. 5 (2014) 4155.
[34] L. Liu, J. H. Perepezko (n.d.), DFT Calculation for Mo Solid Solution With B and Si Addition, (to be published).
[35] G. Hägg, Z. Phys. Chem. B12 (1931) 33.